Journal of Catalysis 282 (2011) 25–34

Contents lists available at ScienceDirect

Journal of Catalysis

journal homepage: www.elsevier.com/locate/jcat

Effect of nanosize on catalytic properties of ferric (hydr)oxides in water: Mechanistic insights

Irina V. Chernyshova *, Sathish Ponnurangam, Ponisseril Somasundaran

NSF I/UCRC Center for Particulate & Surfactant Systems (CPaSS), Columbia University, New York, NY 10027, United States

ARTICLE INFO

Article history:
Received 7 February 2011
Revised 17 May 2011
Accepted 18 May 2011
Available online 6 July 2011

Keywords:
Reaction kinetics
Electrochemical mechanism
Wet catalysis
FTIR
XPS
Nanosize effect

ABSTRACT

Abiotic and biotic processes catalyzed by ferric (hydr)oxide nanoparticles (NPs) in aquatic media underlie many important nanotechnologies including chemical catalysis, biomedical engineering, remediation of contaminants, and clean renewable energy sources. These processes have been extensively addressed in the past and commonly interpreted within the so-called chemical paradigm neglecting semiconducting properties of the NPs. Using batch kinetic measurements coupled with X-ray photoelectron spectroscopy (XPS) as well as a new method that combines *in situ* FTIR spectroscopy and *ex situ* XPS, we study the effect of size on the catalytic oxygenation of Mn(II) in the presence of hematite (α-Fe_2O_3) and ferrihydrite NPs. We find that oxidative catalytic performance of these NPs degrades with decreasing their size. Using Density Functional Theory (DFT) modeling, we show that this unusual trend cannot be rationalized within the traditional chemical paradigm. Given the nanosize-induced changes in the electronic properties of ferric (hydr)oxides and the thermodynamic properties of the system, we demonstrate that the catalytic reaction proceeds through the electrochemical pathway. The new mechanistic insights suggest new interpretation of literature data, open up new possibilities for manipulating technological performance of metal oxides, and conceptually broaden our general understanding of (bio)chemical activity of NPs.

1. Introduction

Ferric (hydr)oxide nanoparticles (NPs) are among the most frequently used (photo)catalysts and sorbents in the environmental remediation and are of interest for nanomedical and solar energy harvesting applications. These NPs are ubiquitous in the environment (oceans, ground and surface waters, sediments, dust, soils, and acid mine drainage) and are present in living organisms, where they play important (bio)geochemical and biological roles. Such a broad scope of (bio)chemical applications as well as the environmental and biological importance has stimulated extensive studies of aquatic chemistry of ferric (hydr)oxide NPs [1,2]. However, the role of nanosize as a control of their (bio)chemical reactivity was recognized only recently [3–11], and the effect of NP size on the redox properties of ferric (hydr)oxides is as yet unclear. On the surface area-normalized basis, goethite (α-FeOOH) microrods were found to be more catalytically active compared to nanorods [8], while acid-assisted dissolution of the latter is faster than of the former [4,12]. The reduction rate of hematite NPs by the dissimilatory iron-reducing bacteria, *Shewanella oneidensis* MR-1, though affected by aggregation, decreases with decreasing NP size [9]. At the same time, a the Mn(II) heterogeneous oxidation is significantly accelerated with decreasing nanosize of hematite from 37 to 7.3 nm [10].

Hematite NPs and ferrihydrite (FH) are among the most abundant ferric (hydr)oxide NPs in the environment [1]. Bulk hematite has a corundum structure with octahedrally coordinated ferric cations. Though this mineral is the most stable iron (hydr)oxide polymorph under oxidizing conditions, it is destabilized with respect to FH in aqueous media in the nanosize regime [13]. FH ($Fe_{10}O_{14}(OH)_2 + \sim H_2O$ in the more ordered form) is a low-crystalline, cation-deficient ferric (hydr)oxide. It contains both tetrahedrally and octahedrally coordinated ferric ions according to Refs. [14,15], though this structure was doubted [16,17]. The nanosize-induced phase transformation into FH results in a decrease in the O 2*p*–Fe 3*d* hybridization, which ultimately brings about localization of valence electrons, destabilization of the valence band, the band-gap opening, and a decrease of the electron affinity of the NPs [7].

Herein, using the Mn(II) heterogenous oxygenation

$$Mn^{2+} + 1/4O_2 + 3/2H_2O \rightarrow MnOOH + 2H^+, \qquad (1)$$

as a model catalytic reaction, we found that the oxidative catalytic capacity of hematite NPs decreases with decreasing NP size at constant pH of the reacting suspension. We show that this result can be accounted for by the so-called electrochemical pathway [18,19] given the changes in the electronic properties, while the previously

---

* Corresponding author.
E-mail address: irina905C@columbia.edu (I.V. Chernyshova).

0021-9517/$ - see front matter © 2011 Elsevier Inc. All rights reserved.
doi:10.1016/j.jcat.2011.05.021

accepted chemical mechanism is inconsistent with the data obtained.

2. Experimental

2.1. Materials

All chemicals were of pure-for-analysis grade or higher, and solutions were prepared from triply distilled water (TDW). All glassware and high-density polyethylene containers were rinsed with 0.1 M HNO_3 and TDW before use.

Highly monodisperse and highly pure hematite NPs of three different average sizes of 7, 9, and 38 nm (H7, H9, H38, respectively) were synthesized by forced hydrolysis as described elsewhere [7]. Importantly, 38- and 9-nm NPs were synthesized using the same protocol as in Ref. [10]. 150-nm hematite (H150) and 2-line ferrihydrite (FH) were acquired from Fisher and Alfa Aesar, respectively, and used as received. All the NPs have similar aspect ratio ranging from 1 to 2. The NPs were extensively characterized. Results of transmission electron microscopy (TEM) are shown in Fig. S1 in Supporting Information. X-ray diffraction (XRD), X-ray photoelectron spectroscopy (XPS), and UV–Vis spectroscopy measurements are reported in Ref. [7]. Except for H7, all the hematite NPs show only hematite XRD patterns, with no lines due to other iron-containing impurity phases. H7 has some admixture of 6-line ferrihydrite. FH is 2-line ferrihydrite with a small admixture of hematite phase. In addition to adventitious carbon, only ferric iron and oxygen were detected by XPS on the hematite NPs, while FH was found to contain Si at the Si/Fe atomic ratio of 0.025. Size, surface area, and surface charging characteristics were also measured. The results are presented in Table 1 and Fig. S2. The values of both point of zero charge (PZC) and iso-electric point (IEP) of 7-, 9-, and 38-nm NPs are within the 7.5–9.5 range typical for hematite NPs synthesized by the hydrolysis of a ferric nitrate/chloride solution and not subjected to drying [1,20–22]. Commercial 150-nm particles are the most acidic (PZC = 6.2), which can be due to either a trace amount of acidic surface impurities or the high-temperature route of their synthesis. FH is characterized by IEP of 7.0 ± 0.1. For comparison, reported values for FH are 7.0 [23], 7.2 [24], 7.5 [25], and 8.5 [26]. Importantly, both PZC and IEP do not change monotonically with increasing the NP size, attaining the maxima for H38.

2.2. Methods

Batch measurements of kinetics of heterogeneous Mn(II) oxidations were run either in 0.04 M HEPES buffer (4-(2-hydroxyethyl)-1-piperazineethanesulfonic acid) or 0.001 M NaCl at [surface OH]/[Mn^{2+}] ratios of 3–25, which were estimated assuming 6 OH groups per nm^2. pH was preset by NaOH (Fisher) and equilibrated overnight upon stirring. Experiments in a 0.04 M HEPES were conducted at constant pH of 7.40 for all hematite NPs and at pH 7.40 and 7.75 for FH. In the case of the non-buffered NaCl suspensions, pH was readjusted to a value in a range of 7.4–9.0, 2 h before the experiment. Mn(II) was added by slowly dripping an appropriate volume of 500 ppm of Mn^{2+} (as $MnCl_2{\cdot}4H_2O$ (Sigma)) to obtain initial concentration of Mn^{2+} between 14.6 and 2 ppm. The reactor volume was 200 ± 2 mL for FH and H150, 123 mL for H7, and 100 ± 2 mL for H9 and H38 in the case of the NaCl suspensions, while volume of all the HEPES-based suspensions in the reactor was 105 ± 2 mL.

All the batch experiments were run under the same stirring conditions for 6–8 h, at room temperature of 23 ± 2 °C, in high-density opaque polyethylene flasks covered with aluminum foil to prevent photolysis. pH was monitored continuously. Aliquots of the test suspension were withdrawn at regular time intervals and analyzed for concentration of Mn^{2+} ions using the formaldoxime spectrophotometric method [10]. Namely, 10 ml of the suspension was placed into a 15 ml polypropylene centrifuge tube. After 15 min of centrifugation, 6 ml of the colorless (as determined by UV–Vis spectrophotometry) supernatant was carefully extracted from the tube and mixed with 1.2 mL of formaldoxime reagent and 3 ml of 5 M NaOH for UV–Vis spectrophotometry after aging for the same time of 1 h. Total time of the Mn^{2+} interaction with NPs was taken as the time lasted from the addition of Mn^{2+} into the suspension to the time when the supernatant was extracted. Dissolved Fe(II) in the filtrate was always below sensitivity of the ferrozine method [9]. Concentration of H7, H9, and H38 in suspensions was determined UV–Vis spectrophotometrically based on calibration curves obtained on dried and redispersed NPs as well as on the as-synthesized suspensions for which concentrations were calculated from loadings of ferric salts.

In situ FTIR spectroscopic measurements were performed on the NPs deposited onto a ZnSe internal reflection element (IRE) (10 internal reflections, angle of incidence 45°) in a 10^{-2} M carbonate buffer in the horizontal attenuated total reflection (HATR) geometry. A Perkin-Elmer Spectrum 100 FTIR spectrometer equipped with an MCT detector, and a HATR accessory equipped with a closed cell with volume of 3 mL was employed. A particulate film of NPs was deposited using 120 μL of a ~250 g/L suspension onto the IRE, which results in surface density of the NPs of ~7 mg/cm^2. The deposited layer was air-dried and then rinsed several times with water to remove any loose or detached particles. The layer was equilibrated for at least 1 h with the buffer being changed manually every 10 min. Afterward, a fresh portion of the buffer was added and the background spectrum was measured. Then, the buffer was replaced with the buffer containing Mn(II). The sample spectra were measured for 5–6 h at ~1-h time intervals. The Mn(II) solution in the cell was refreshed after 1 and 2 h from the start. The spectra were collected at 300 scans at a resolution of 4 cm^{-1} and represented in the absorbance scale.

To determine the oxidation state of sorbed Mn(II) as well as to quantify adsorption density of manganese, samples collected after the batch and *in situ* FTIR experiments were analyzed by XPS. We used a Perkin-Elmer 5400 instrument using nonmonochromatic Al Kα X-rays with pass energies of 17.6 eV at a take-off angle of 45° at pressures of less than 4×10^{-9} Torr, calibrated using the Au($4f_{7/2}$) peak at 84.0 eV. Regional XPS scans from 10 to 50 eV windows widths were collected at 0.1 eV steps. The Mn/Fe atomic concentration ratios were evaluated using the Mn $2p_{3/2}$ and Fe $2p_{3/2}$ peaks and PHI atomic sensitivity factors. The Shirley function was used to subtract the background.

The XPS spectra were reproduced in terms of peak widths and shapes as well as surface atomic concentrations, within the experimental error of the method. However, the peak position was reproduced only if binding energies (BE) were corrected for the charging effect by assuming a common BE for the O 1*s* core-level electrons of lattice oxygen, which was taken to be 529.9 eV. Such referencing of BE is used in some of previous XPS studies of ferric

Table 1
Size, surface area, and surface charging characteristics of ferric (hydr)oxide NPs.

Sample	Average particle size (TEM) (nm)	BET (m^2/g)	PZC	IEP
FH	2–4	180	8.0 (7.1[a])	7.1
H7	7	154.4	8.8	8.9
H9	9	128.3	8.8 (8.5[a])	8.5
H38	38	37.0	9.2	9.3
H150	150	9.5	6.2 (6.2[a])	7.0

[a] In air-saturated electrolyte.

oxides [27,28], because common referencing to the C 1*s* signal of hydrocarbon contamination can be ambiguous [29]. Besides, there is no convincing evidence so far that the O 1*s* peak position of transition metal oxides is significantly affected by variations in cation site occupancy [30].

Density Functional Theory (DFT) calculations were performed using the exchange–correlation functional Perdew–Burke–Ernzerhof (PBE) Generalized Gradient Approximation (GGA) as implemented in Dmol, Material Studio (Accelrys Inc., San Diego, California). Numerical basis set of Double Numerical Polarization (DNP) with double polarization functions capable of accurate description of hydrogen bonding was employed. Energy optimization was performed under symmetry unrestricted and spatially unconstrained conditions. Spin unrestricted wave functions were employed. Hydrated Mn(II) was modeled by $Mn(OH_2)_6^{2+}$ and $Mn(OH)(OH_2)_6^{+}$ octahedra. The effects of polarizability of the immersion medium were neglected (calculations were performed at dielectric constant of 1). Such simplifications are justified by the purpose of current study, which is to determine variations in the HOMO–LUMO levels with bonding strength. To vary the Mn(II)O-Fe bond strength, each of the Mn(II) species was bound to a Fe(III) or Fe(II) octahedron in (a) monodentate or (b) bidentate chelating form, and the oxidation state of the iron cation was taken as either +2 or +3. Mulliken population analysis was performed in order to obtain the orbital occupation of Mn(II) ion both in dissolved and adsorbed state.

3. Results

3.1. Batch kinetic and XPS measurements

We measured kinetics of the Mn(II) oxygenation in the presence of hematite NPs with mean sizes of 7, 9, 38, and 150 nm in both 0.04 M HEPES at pH 7.4 and 0.001 M NaCl at pH 7.0–7.15. The results revealed that the normalized pseudo-first order rate constant of the reaction, k'_{obs}, decreases with decreasing NP size (Fig. 1a). The reason for the opposite trend reported in the literature [10] can be differences in the pH values naturally established in unbuffered suspensions of different catalysts under the conditions of Ref. [10] (see Supporting Information for more detail). As seen from Fig. 1b, smaller NPs are also characterized by lower surface concentration of the manganese sorbed during the first 30–60 min. As this time interval is typical for the Mn(II) sorption on ferric hydroxides [31], this fact indicates that larger hematite NPs have higher sorption capacity, in agreement with published data [11,12,7].

For comparison, we also evaluated the catalytic properties of FH (∼4-nm amorphous precursor of hematite). In the presence of these NPs, no statistically meaningful change in the Mn(II) concentration is detected at pH 7.0–7.4, under both unbuffered (Figs. S3c) and buffered (not shown) conditions. However, the reaction propagates at higher pH of 7.75, the rate being comparable to that observed on 9-nm hematite at pH 7.4 (Fig. S3 and Table S1).

The XPS analysis of surfaces of the reacted NPs (Table S4 and Fig. S8) confirms that the Mn/Fe atomic ratio increases with increasing NP size. This confirmation is important since the macroscopic data based on measurements of the solution depletion include an intrinsic error caused by the normalization of the observed rates by the BET surface area of NPs. This error is due to the difference between the BET and effective surface areas of suspended NPs, which is affected by their aggregation state [8,32]. Moreover, this state can substantially vary in the course of the heterogeneous reaction. The XPS analysis of the reacted NPs is also free from another potential artifact of the macroscopic data caused by experimental limitations in separating NPs from solution.

The low signal-to-noise ratio in both the Mn 2p and Mn 3s photoemission does not allow inferring the NP size effect on the oxidation state of manganese. The presence of the distinct Mn $2p_{3/2}$ satellite in the Mn 2p core-level spectra (Fig. S8d) suggests (*vide infra*) that the reaction product is dominated by Mn(II) for all the NPs. Interestingly, the effect of the Mn(II) oxygenation on the NPs was very little except for 9-nm hematite. The latter is partially reduced during the catalytic redox reaction, as follows from the Fe 2p spectrum (Fig. S8a).

3.2. In situ FTIR-ex situ XPS method

To verify that the reaction rate of the catalytic Mn(II) oxygenation decreases with decreasing NP size and to further explore the reaction details, we employed a new *in situ* FTIR–*ex situ* XPS spectroscopic approach; Time-dependent *in situ* FTIR spectra were measured to follow the reaction kinetics, while the reacted NPs collected at the end of each kinetic run were analyzed using XPS. The Mn/Fe atomic ratios evaluated from the XPS peak areas were used to convert the time-dependent FTIR peak intensity into the time-dependent Mn/Fe atomic ratios. The suggested method also

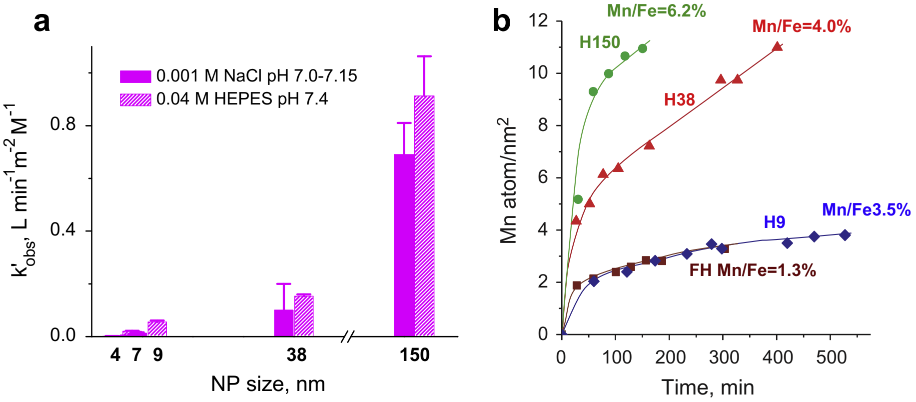

Fig. 1. Kinetics of catalytic Mn(II) oxygenation on ferrihydrite (FH) and hematite NPs in 0.04 M HEPES at pH 7.4 and 0.001 M NaCl at pH 7.0–7.15 (see Table S2 for more detail): (a) Normalized rate constant $k'_{obs} = k_{obs}/(SA \cdot m \cdot [Mn^{2+}])$, where k_{obs} is the observed pseudo-first order rate constant, SA = BET surface area, $[Mn^{2+}]$ = initial molar concentration of Mn(II), and m = concentration of NPs in g/L. Uncertainties represent the sum of error of the linear fit and standard deviation determined from duplicate experiments. (b) Time dependence of Mn adsorption density on NPs in HEPES at pH 7.4 (hematite) and pH 7.75 (FH), which was calculated from the pseudo-first order plots (Fig. S3). Also shown is Mn/Fe atomic ratio measured by XPS on the last probe in the series.

provides direct information about the oxidation state as well as the composition/structure of both the reaction products and the catalyst. Another its advantage is the lack of the inherent limitations mentioned above of the solution depletion method.

The measurements were performed in a 10^{-2} M carbonate buffer at pH 8.55 (Fig. 2) and in a 10^{-3}M carbonate at pH 8 (Fig. S6) and pH 9 (Fig. S7). The initial Mn(II) concentration was selected to be either higher (80 ppm at pH8) or lower (10 and 27 ppm at pH9 and 8.55, respectively) than concentration of the reacting Fe–OH sites (calculated assuming the site density of 6 sites/nm^2 (Ref. [10])).

The *in situ* FTIR spectra (Figs. 2, S6, and S7) of the reaction product that is formed in the initial stage of the reaction exhibit two strong broad absorption bands at ~1480 and 1365 cm^{-1} as well as a weak sharp band at 1070 cm^{-1}. These bands can be attributed to the stretching vibrations νCO_3^{2-} of adsorbed $MnCO_3$-like species based on comparison with the spectra of the reference compounds (Fig. 2d). With elapse of time, a new broad feature at ~1090 cm^{-1} is developed and further split into two narrow components at 1155 and 1090 cm^{-1} assignable to the bending δMn–OH mode of manganite γ-MnOOH. The manganite bands are more pronounced in the spectra of coarser NPs, implying that coarser NPs convert a larger fraction of the initially (ad)sorbed $MnCO_3$-like species into γ-MnOOH. Accordingly, compared to the δMn–OH bands, intensities of the νCO_3^{2-} bands are lower in the spectra of coarser NPs, suggesting that a smaller fraction of $MnCO_3$ remains in the reaction product.

To compare kinetics of the reaction on the different NPs, we converted the time-dependent 1090-cm^{-1} band intensity into the time-dependent Mn/Fe atomic ratio using the Mn/Fe atomic ratio measured by XPS on the reacted samples. The spectroscopy-based dependences directly show that the oxidative catalytic properties of hematite are improved with increasing NP size (Figs. 2e, S5d, and S6d).

An additional evidence of the stronger catalytic properties of larger NPs is provided by analysis of the Mn 3s and Mn 2p photoemissions, which are sensitive to the oxidation state of manganese. A signature of a higher oxidation state of the adsorbed manganese is a lower splitting between the ^{7}S and ^{5}S multiplet components at ~84 and 90 eV, respectively, in the Mn 3s spectra (Fig. S10) [29]. As seen from Fig. 3, the ^{5}S–^{7}S splitting decreases with increasing NP size from 6.2 eV to 5.5 eV as NP size increases from 9 to 150 nm. This trend is also observed at pH 9 (Fig. S9). Taking into account the multiplet splitting of 6.2 eV for rhodocrosite ($MnCO_3$) [29], MnO [33], and manganese ferrite ($MnFe_2O_4$) [34], 5.6 eV for Mn_3O_4 [33] and 5.4–5.3 eV for manganate (γ-MnOOH) and Mn_2O_3 [29,35], one can conclude that the average oxidation state of Mn on 9, 38, and 150-nm hematite is +2.0, 2.3, and +2.8, respectively. (These values are obtained using the oxidation state correlation shown in Fig. S10.)

Features of the Mn 2p photoemission support the above conclusion. The main peaks at 642.2 and 653.9 eV in the Mn 2p photoemission of the reacted NPs are due to the Mn $2p_{3/2}$ and Mn $2p_{1/2}$ spin–orbit components, respectively (Fig. 3d). The Mn $2p_{1/2}$ component is accompanied by the Mn $2p_{1/2}$ shake-up charge transfer satellite at 664 eV, while the Mn $2p_{3/2}$ satellite is not observed due to its overlap with the Mn $2p_{1/2}$ main peak. Such a spectral picture is typical for Mn(III) and Mn(IV) (hydr)oxides [36–38]. In contrast, a prominent Mn $2p_{3/2}$ satellite is typical for Mn(II)-containing compounds as well as for tetrahedrally coordinated manganese with strong O 2*p*–Mn 3*d* hybridization [34,38–40]. As NP size increases, intensity of the Mn $2p_{1/2}$ satellite increases, which signifies a gain in the oxidation state of the cation. A slight shift of the Mn $2p_{3/2}$ peak to lower binding energies also points to that the lowest

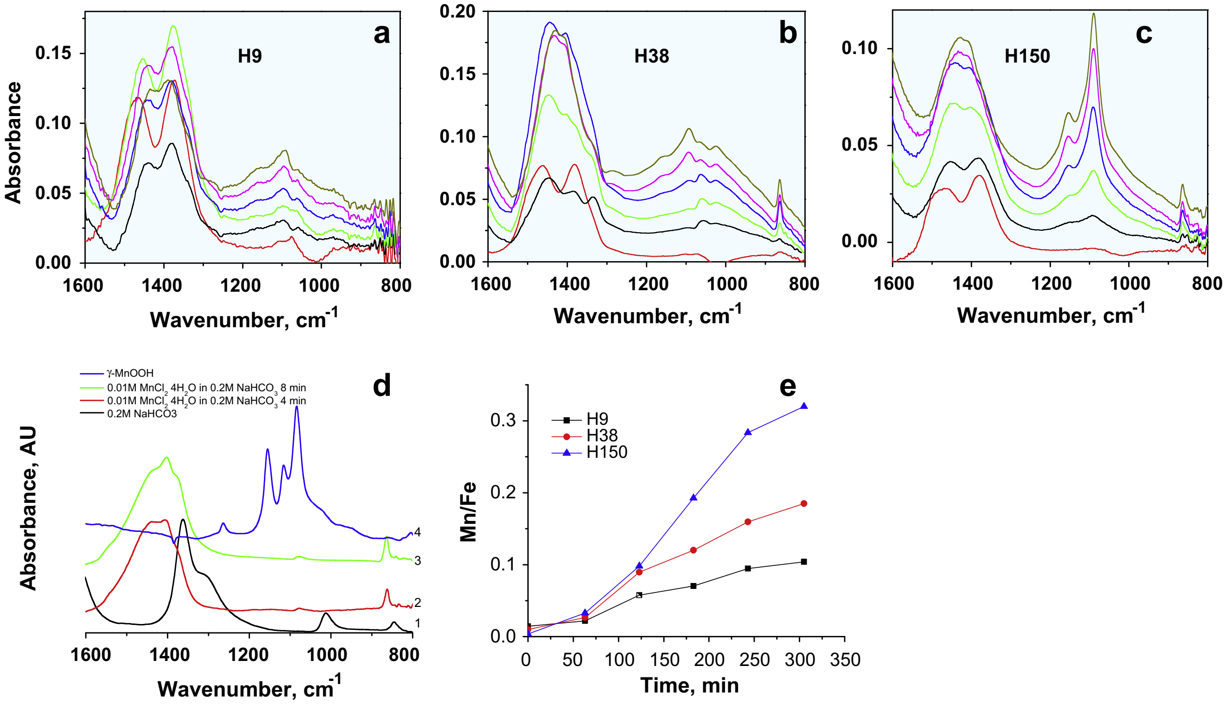

Fig. 2. Time-dependence of *in situ* FTIR spectra of (a) 9-nm, (b) 38-nm, and (c) 150-nm hematite NPs in a 27 ppm Mn(II) solution in a 10^{-2} M bicarbonate buffer of pH 8.55. The bottom spectrum was measured 2–3 min after adding Mn(II) into the FTIR cell. Time interval between the spectra was 1 h. Time increases from bottom (red) to top spectrum. (d) HATR spectra of reference compounds: (1) 0.2 M solution of $NaHCO_3$, (2) 0.01 M $MnCl_2·4H_2O$ in 0.2 M $NaHCO_3$ 4 min of aging, (3) 0.01 M $MnCl_2·4H_2O$ in 0.2 M $NaHCO_3$ 8 min of aging, (4) diffuse reflectance spectrum of dry synthetic γ-MgOOH. All spectra are offset for better clarity. (e) Adsorption density of Mn evaluated from the manganite peak intensity at 1090 cm^{-1} and the Mn/Fe atomic ratio measured by XPS on the reacted NPs collected at the end of each kinetic run. Lines are drawn to guide eye. (For interpretation of the references to color in this figure legend, the reader is referred to the web version of this article.)

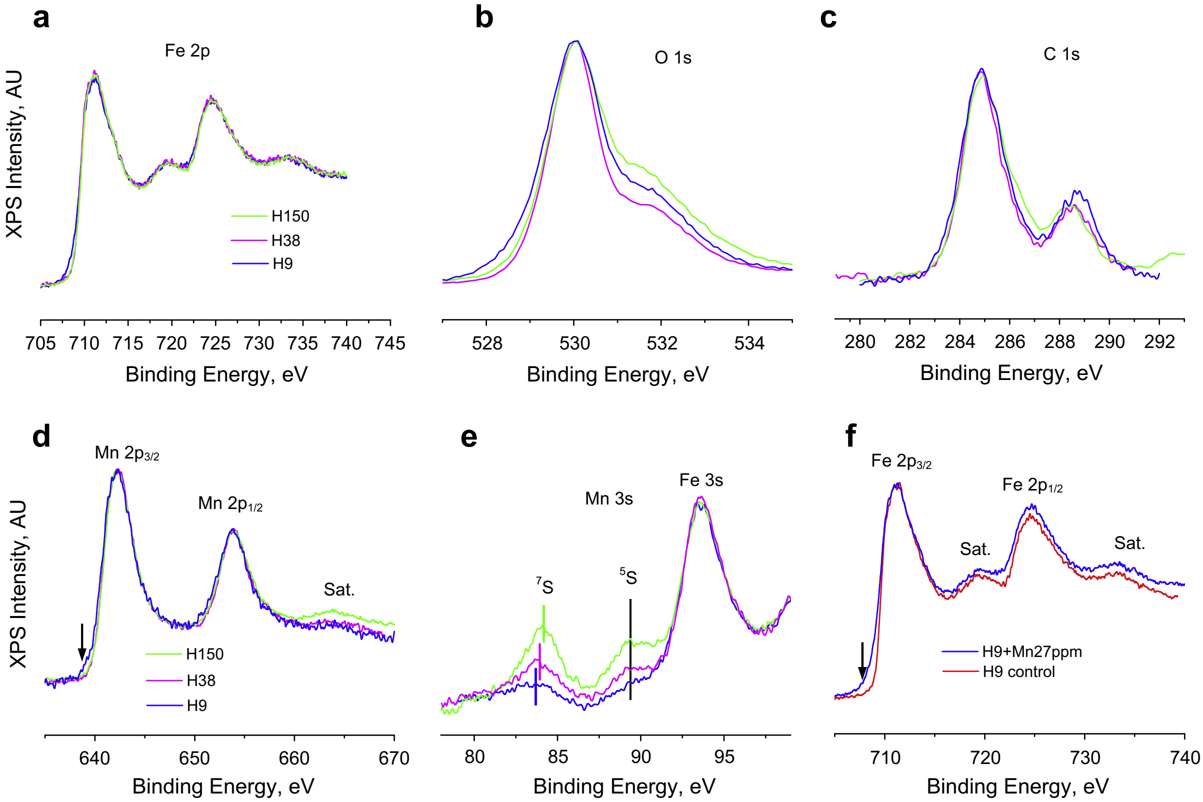

Fig. 3. (a) Fe 2*p*, (b) O 1*s*, (c) C 1*s*, (d) Mn 2*p*, and (e) Mn 3*s* and Fe 3*s* XPS core-level spectra of FH and 9, 38, and 150-nm hematite collected after reaction with 27 ppm Mn(II) in 0.01 M $NaHCO_3$ at pH 8.55 in the *in situ* FTIR cell (Fig. 2): H9 (blue), H38 (magenta), and H150 (green). (f) Comparison of the Fe 2*p* spectra of 9-nm hematite before (red) and after (blue) interaction with Mn(II). Shoulder at low binding energy (marked by arrow) indicates that 9-nm hematite is reduced during the reaction. (For interpretation of the references to color in this figure legend, the reader is referred to the web version of this article.)

oxidation state of Mn on 9-nm as compared to 38-and 150-nm hematite.

Finally, it is worth noting that the Fe $2p_{3/2}$ peak of the reacted NPs exhibits a shoulder at lower binding energies (marked by arrow in Figs. 3f and 4), suggesting the presence of Fe(II). Moreover, the Fe $2p_{3/2}$ peak of 150-nm (not shown) and 38-nm (Fig. 4) hematite is characteristically split (marked by lines), which is due to the effects of crystal field and spin–orbit coupling between the 2p core hole and unpaired 3d electrons of the photoionized ferric cation [41–43]. The subpeak at lower binding energy has a lower intensity in the case of the reacted NPs. A similar effect was previously observed for ferric cations on a hematite surface compared to the bulk and attributed to a reduction of the crystal field [44]. If so, surface cations that have interacted with Mn(II) experience a weaker crystal field, which can be caused by a distortion of their octahedral coordination or by a decrease in the coordination number. This observation allows concluding that manganese forms inner-sphere surface complexes with hematite upon the adsorption.

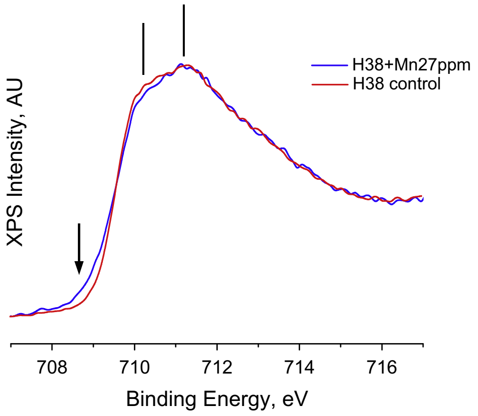

Fig. 4. XPS Fe 2p3/2 peak of (red) initial 38-nm hematite and (blue) 38-nm hematite reacted with 27 ppm of Mn(II) at pH 8.55 for 5 h in the *in situ* FTIR cell (Fig. 2). (For interpretation of the references to color in this figure legend, the reader is referred to the web version of this article.)

3.3. DFT calculations

To discriminate between possible mechanisms of the catalytic reaction, DFT calculations were performed to explore how the HOMO–LUMO energies of a hydrated Mn(II) ion change upon varying the strength of its binding to a hydrated iron octahedron in order. The results (Fig. 5) show that strengthening of the Mn(II)O–Fe bond results in a more negative value of the HOMO energy of the Mn(II) complex and a lower Mn 3d electron density. This implies that stronger Mn(II) complexes are harder nucleophiles (weaker electron donors) than the weaker ones. Similar results were obtained in a DFT study of the electronic properties of bridging bidentate and monodentate adsorption forms of formic acid on the $(10\bar{1}0)$ ZnO surface modeled as a slab [45].

4. Discussion

4.1. Reaction mechanism

The NP size-induced changes in the catalytic redox properties of ferric (hydr)oxides have previously been discussed exclusively within the *chemical* paradigm [46–48] in terms of variations in crystallographic facets, aggregation, surface hydration, basicity of

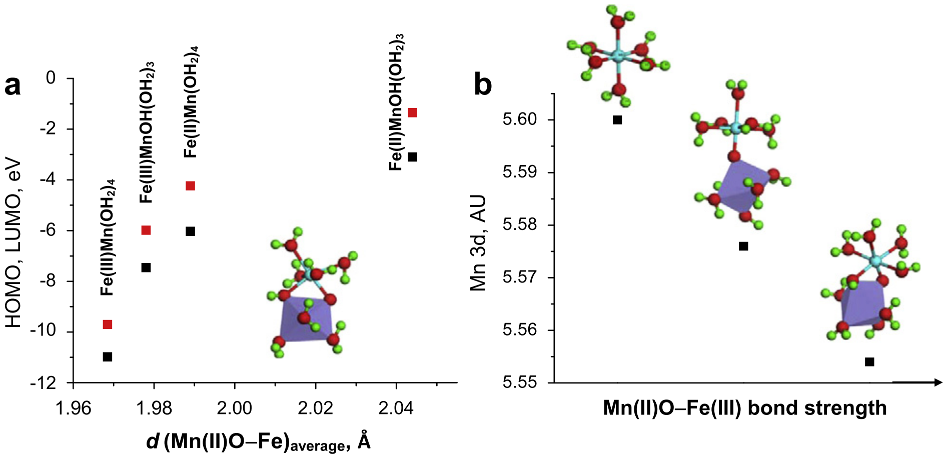

Fig. 5. Dependence of (a) HOMO and LUMO energies on the average Mn(II)O-Fe bond length in chelating complexes of $Mn(OH_2)_6$ and $MnOH(OH_2)_5$ with $Fe(II)(OH_2)_6$ and $Fe(III)(OH_2)_6$ octahedra and (b) variations in Mulliken population of Mn 3d electrons in free, mononuclear monodentate and chelating complexes of $Mn(OH_2)_6$ with $Fe(III)(OH_2)_6$ octahedra.

the NPs, and surface texture (relative concentration of weakly and strongly adsorbed complexes) [8–10]. This paradigm considers that both the reduction and oxidation half-reactions take place at the same adsorption site or two neighboring adsorption sites and neglects semiconducting properties of the NPs, though the details vary (e.g., the reaction mechanism can be of the Rideal or Langmuir–Hinshelwood type). The kinetics of electron transfer (ET) in such a process is determined by the relative positions of the HOMO and LUMO of the reactants. The catalytic effect of the surface is attributed to accumulating the reactants and decreasing the activation energy for ET [49]. In particular, adsorption is believed to increase the electron density on the reductant thereby decreasing its formal reduction potential and thus making it more prone to electrophilic attack. Moreover, the stronger the adsorption, the lower is the activation energy barrier for ET [31,46,47,50,51].

The macroscopic acid–base properties (Table 1 and Fig. S2b) suggest that 38-nm hematite is most basic among the NPs used in the study. Hence, if the chemical paradigm were valid, the highest rate of the Mn(II) oxidation and the highest fraction of the oxidation product MnOOH would be observed on these nanoparticles because higher basicity of their surface oxygens would result in a lower redox potential of the attached reducing cation [10,31,50–52]. However, the highest oxidative capacity is demonstrated by 150-nm hematite. Another possible interpretation of our results within the chemical paradigm could be that an increase in NP size is accompanied by a strengthening of the Mn(II) bonding to their surface [31], which reduces the reorganization energy penalty for ET from adsorbed Mn(II) to O_2 [10]. In fact, available data suggest that the adsorption affinity of hematite trends to increase with increasing NP size [7,53]. However, as follows from our DFT modeling results (Fig. 5), the electron-donating capacity of stronger Mn(II) complexes is lower. Therefore, if the chemical pathway was the case, the reaction would slow down with increasing NP size, which is opposite to what is observed. Furthermore, the surface area normalized reaction rate monotonically decreases with decreasing NP size despite the significant difference in the morphology of the 38-nm hematite (Fig. S1) and hence in the proportion of the exposed strongly vs. weakly adsorbed surface sites. Provided the anodic reaction is the rate determining step, this fact can imply that kinetics of electron injection is faster than that of the formation of a stable surface complex. We also reject the possibility of the catalysis by elevated pH in the diffuse layer due to a higher concentration of OH^- counter-ions attracted to more positively charged NPs [54] based on the surface charging characteristics of the NPs (Table 1 and Fig. S2). In this case, the highest reaction rate would also be observed for the most basic 38-nm hematite. Finally, the chemical paradigm is unable to interpret why 9-nm hematite is reduced while smaller FH NPs are not. Hence, this paradigm is considered to be untenable for aquatic catalytic reactivity of hematite.

A specific feature of the alternative, *electrochemical* mechanism is the spatial separation of the oxidation and reduction half-reactions, which are electrically coupled by charge transfer within either the interior or surface of the catalyst [18,19] (Fig. 6). The electrochemical mechanism can be considered as a modification of the Mars-van Krevelen, or redox mechanism that is generally accepted for the gas-phase catalysis by metal oxides [55]. This pathway can be energetically more favorable compared to the chemical pathway provided (i) the product of heterogeneity of the surface potential $\Delta\Psi_s$ and the NP conductivity is sufficient to support ET between the anodic and cathodic reaction spots and (ii) the condition of the optimum exoergicity is satisfied [56]. The latter implies that the standard redox potentials of the redox half-reactions should match the position of the conduction or valence band to allow both electron injection into the catalysts and ET to the oxidant. Hence, the electrochemical model takes into consideration the semiconductor side of the electric double layer through incorporating new variables such as the position of the Fermi level relative to the conduction and valence band edges at the semiconductor surface, the rectifying properties of the space charge layer, and conductivity of the semiconductor. The difference between the

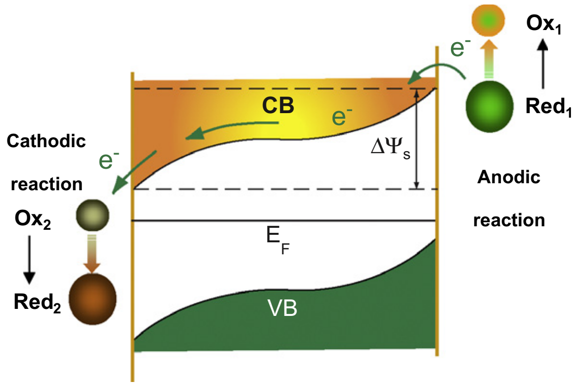

Fig. 6. Conceptual scheme of electrochemical mechanism of redox reaction Ox2 + Red1 → Ox1 + Red2. FL = Fermi level, VB = valence band, CB = conduction band, $\Delta\Psi_s$ = gradient of surface potential.

electrochemical and gas phase redox mechanisms is in new reaction controls such as reorganization energy of the hydration shell, the space charge layer in the oxide, and the structure and thickness of the electrical double layer. In addition, ET can also be accomplished through the outer-sphere complex pathway.

The electrochemical route, which is generally accepted for aquatic chemistry of semiconducting sulfides [18,57–59], was recently suggested for catalysis of gold [60] and semiconducting metal oxide [19] NPs in water. Below we show that, as opposed to the chemical paradigm, the electrochemical mechanism is capable of consistently explaining: (i) why larger hematite NPs are better (per unit surface area) catalysts compared to more defective smaller counterparts to which higher reactivity could intuitively be ascribed; (ii) why ferric (hydr)oxide NPs of certain size can be reduced during the catalytic process, and also (iii) the previously reported dependence of the growth pattern of the Mn(II) oxygenation product on conductivity of the catalyst [29].

Reaction (1) is split into the oxidation and reduction half-reactions as:

$$\equiv \mathrm{S}-\mathrm{MnCO}_{3\mathrm{ads}}+2\mathrm{H}_2\mathrm{O}\rightarrow\equiv \mathrm{S}-\mathrm{MnOOH}_{\mathrm{ads}}+\mathrm{CO}_3^{2-}+3\mathrm{H}^+ + e, \qquad (2)$$

and

$$\mathrm{O}_2+4e+4\mathrm{H}^+\rightarrow 2\mathrm{H}_2\mathrm{O}, \qquad (3)$$

respectively, where e denotes electron, though the actual reaction pathway can be much more complex.

To show that coupling of processes (2) and (3) is thermodynamically possible through the conduction band of highly crystalline 150-nm hematite particles but can be hindered in the case of defective NPs, we model the energetics of these two extreme systems at pH 7.4 (Fig. 7). To evaluate the electron energy of 150-nm hematite particles, we assume that these particles have semiconducting properties of bulk hematite, which is a reasonable approximation based on similarity of their structural [13] and electronic [7] properties. We also neglect the possible effects of aggregation on the electronic properties [19]. Hence, energy levels of 150-nm hematite correspond to those of ideal n-type semiconductor with band gap of 2 eV [7] and an energy gap of 0.15 eV between the flat-band potential E_{fb} of −0.10 V and the bottom of the conduction band [1,7,61]. At E_{fb} in the absence of dissolved oxygen (Fig. 7a), the electrochemical potential of the redox couple MnOOH/$MnCO_3$ is in the energy gap of 150-nm hematite and below the Fermi level (the electrochemical potential of electrons in a solid), E_F. Therefore, injection of electron from $MnCO_3$ into hematite is thermodynamically forbidden under such conditions.

If oxygen is fed to the reactor, it is preferably adsorbed on the most negatively charged facets or surface defects of the catalyst. The relative positions of the conduction band edge, the Fermi level, and potential of half-reaction (3) allow the adsorbed oxygen to be reduced by capturing free electrons of hematite (Fig. 7b). Then, electrons will flow from the semiconductor to the solution until equilibrium is established. At the equilibrium, the 150-nm hematite particle is charged positively and it's the Fermi level is equal to the electrochemical potential of the oxygen reduction [half-reaction (3)]. Under such conditions, the redox potential of oxidation half-reaction (2) already occurs above E_F, and ET from Mn(II) to hematite becomes thermodynamically possible (Fig. 7b). Since the MnOOH/$MnCO_3$ redox potential is below E_{CB}, we speculate that the catalytic reaction can be mediated by surface states (undercoordinated ferric cations). Indeed, undercoordinated surface atoms have different energies compared to the counterparts in the semiconductor bulk because of experience a weaker Madelung potential. As atoms get more undercoordinated, the cation (oxygen) levels shift toward lower (higher) energies, as expected from the reduction of the Madelung potential. This means that at surfaces, the acidic strength of a cation and the basic strength of an oxygen increase [62]. Alternatively, electrons can tunnel across the interfacial barrier under the strongly electron-depletion conditions [63]. Finally, the Mn(II) oxidation can be accomplished by holes since it is accelerated upon UV irradiation (not shown). If injected, the electron will be moved away by the potential drop in the space charge layer from the anodic spot toward the cathodic spot where an O_2 molecule can consume it (Fig. 7b). Therefore, the net reaction (2) can proceed through the electrochemical route.

Importantly, as seen from Fig. 7a and b, the reduction of well-crystalline hematite by Mn(II)

$$\mathrm{Fe}_2\mathrm{O}_3+6\mathrm{H}^+ + 2e\rightarrow 2\mathrm{Fe}^{2+}+3\mathrm{H}_2\mathrm{O}, \qquad (4a)$$

or

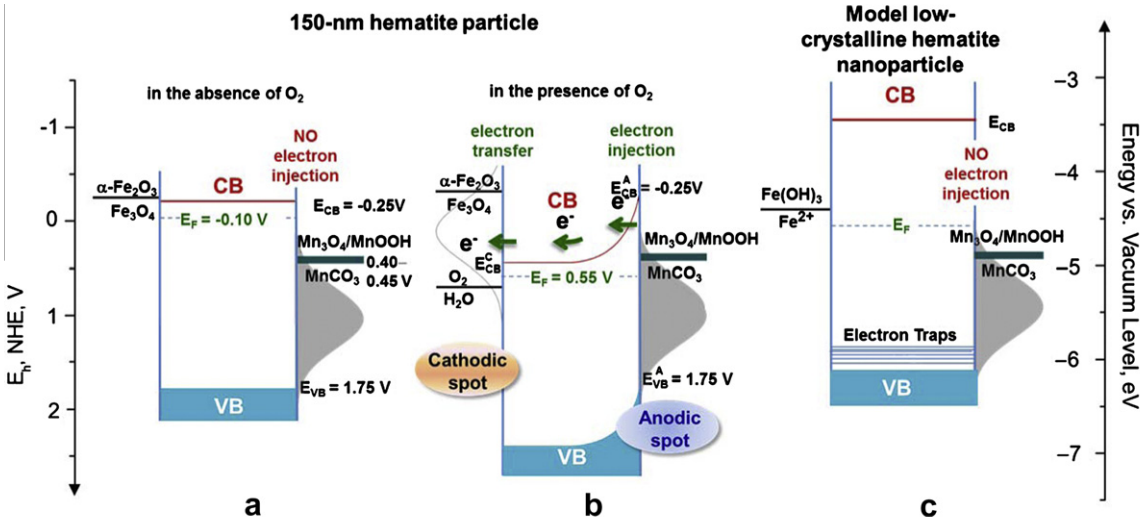

Fig. 7. Schematic diagram of electron energetics of (a) 150-nm hematite at flat-band potential E_{fb} of −0.10 V (NHE) in the absence of dissolved oxygen; (b) 150-nm hematite at open-circuit potential under air-saturated conditions in the presence of 10 ppm Mn(II) as $MnCO_3$; (c) a virtual low-crystalline hematite NP at E_{fb} of 0.15 V (NHE) in the absence of dissolved oxygen. Reduction potentials [19,78] of Mn_3O_4/$MnCO_3$, O_2/H_2O and Fe(III)/Fe(II) couples are shown for pH 7.4. VB = valence band, CB = conduction band, E^A_{CB} and E^C_{CB} = conduction band edges at anodic and cathodic spots, respectively, E^A_{VB} = valence band edge at anodic spot. Shaded and empty Gaussians depict electron level distribution of dissolved Mn(II) and O_2, respectively, with a typical reorganization energy of 1 eV [79].

$$3Fe_2O_3 + 2H^+ + 2e \rightarrow 2Fe_3O_4 + H_2O, \quad (4b)$$

is precluded both in the absence and presence of oxygen because redox potential of reactions (4) is above the bottom of the conduction band.

The nanosize-driven changes in the structural [13] and electronic [7] properties of hematite allow interpreting their poorer oxidative catalytic activity as follows. A decrease in size/crystallinity of hematite NPs is known to produce electron-acceptor states (Fe-vacancies) [64–66]. The resulting lower concentration of free electrons shifts E_{fb} downwards compared to that of the well-crystalline oxide increasing the energy gap between E_F and the conduction band edge, as shown schematically in Fig. 7c. Therefore, upon equilibrating with the O_2/OH^- redox couple, smaller hematite NPs will develop a lesser band bending. An additional contribution to this effect is expected from their small size compared to a typical thickness of the space charge layer of ~100 nm, which precludes development of the space charge layer. The resulting decrease in the gradient of the electrostatic potential inside the NP hinders ET from the anodic to the cathodic spot (Fig. 6). Finally, a decrease in crystallinity of hematite is accompanied by an opening of the band gap of the semiconductor, which suggests a higher energy for its conduction band edge [7]. The upward shift of the conduction band hampers the electron injection from the reducing species as the overlap of the electron levels diminishes. Along with the decreased concentration of free electrons and higher concentration of charge traps, these changes in the electronic properties slow the heterogeneous redox reaction.

A slowing of the oxidation process results in negatively charging of the catalyst, which shifts its conduction band upward. This shift makes reactions (4) possible, which explains corrosion of hematite NPs observed in the FTIR–XPS experiments as well as of 9-nm hematite in the batch experiments. Interestingly, we did not find Fe(II) on the smallest (~ 4 nm) FH NPs using XPS as well as in the FH suspensions reacted with Mn(II) using the ferrozine method. This fact suggests that there is no kinetic obstacles for the Fe(II) ions produced by reactions (4) to be reoxidized by dissolved oxygen, resulting in phase transformation of FH. In fact, phase transformation was reported for the Fe(II) oxygenation [22] and Fe(II)-mediated reduction of U(VI) [67] on FH. Thus, given the variation in the electronic properties of the NPs and the thermodynamic properties of the system, the redox activity of hematite NPs is more likely to be driven by the electrochemical than chemical mechanism.

4.2. Consistency of the electrochemical concept with reported data

The electrochemical concept of reactivity of hematite NPs is strongly supported by the observation of the electric current between different facets of a hematite macrocrystal observed during the concerted dissolution-growth of these facets under anaerobic conditions in the presence of oxalic acid and Fe(II) [68].

According to this concept, the autocatalytic regime of the Mn(II) oxygenation becomes energetically more favorable compared to the heterocatalytic regime when the activation barrier for ET through the oxidation product becomes lower than through the primary catalyst. Since conductivity of MnOOH significantly increases with both dehydration and oxidation of the hydroxide [69], such a redirection of the ET route can be anticipated when the degree of the Mn(II) oxidation is higher, namely, on larger hematite NPs.

The above arguments offer a new insight into the catalyst-dependent growth patterns of the reaction products [29]. The Mn(II) oxygenation was found to be initiated at the base of surface steps of hematite and is developed as a substrate-controlled process through the terrace, in contrast to albite on which the growth is controlled by the initial Mn(III) precipitate [29]. This difference was previously interpreted within the chemical paradigm as a result of different chemical reactivity of surface sites of the minerals [29]. However, in lieu view of the above discussion, the reason for the different growth patterns can be different conductivity of the catalysts. In fact, heterocatalytic regime is expected to be energetically more preferable on hematite due to its much better conductivity compared to the initial product, Mn(II)Mn(III) oxocarbonate [69]. However, for insulating albite, the reaction can propagate only in the autocatalytic regime.

Ferric (hydr)oxides have similar electronic structures [70] and similarly accept electron from adsorbed Fe(II) [68,71,72]. On this basis, it can be suggested that the electrochemical type of (bio)chemical activity is common for this class of semiconductors. If so, the lower catalytic activity of goethite nanorods compared to microrods [8] can be due to higher ionicity and larger band gaps of the former, which can be concluded based on the reported electronic spectra [12]. The higher reductive potential of electrons captured by smaller NPs (which is due to the higher energy of their conduction bands) is expected to contribute to the enhanced reductive dissolution of smaller ferric hydroxide NPs by hydroquinone [73] as well as to the acid-promoted dissolution of nanogoethite compared to microgoethite [4,12], in addition to the conventional effect of the increased surface area. The electrochemical mechanism also allows attributing the morphology-selective dissolution pattern of goethite nanorods [4,74] to the difference in the surface potential of the different crystallographic facets [75], by analogy to hematite [68].

4.3. Implications

So far, experimental data on reactivity of metal oxides have mainly been interpreted within surface complexation models of the solution side of the interface [46–48], though both the importance of the electronic structure of the adsorbent surface for the adsorbent–adsorbate hybridization has been recognized [76,77]. The new, electrochemical approach to aquatic chemistry of semiconducting metal oxides implies the priority of energetics of the solid–water interface and electronic properties of the solid over the structural details of the solid surface in both reactivity and selectivity of the solid. Indeed, there is no doubt that the surface structure, which depends on the synthesis history and exposed crystallographic planes of the solid, affects the molecular recognition mechanisms. At the same time, this molecular structure is reflected in the electronic structure of the interface that in turn can be manipulated through changing the redox potentials of the solid and/or the solution. The former can be done, for example, by doping the solid with an appropriate element or employing the nanosize, aggregation, or deposition [19] effects. Also, the electrochemical concept predicts that, the average size being the same, the NPs with higher morphological inhomogeneity will be more redox active.

Based on our results and generality of the redox mechanism for the dark catalytic activity of semiconducting metal oxides in gas phase [55], the electrochemical mechanism can be expected to be common for this class of solids in electrolytes. If so, along with the conventional physico-chemical characteristics of the solution side of the interface, the semiconducting properties of the catalysts should be involved in modeling and used for manipulating their aquatic chemistry in the dark. Given the similarity of the electrochemical and photocatalytic mechanisms, the semiconducting properties to be introduced in the area include positions of the conduction and valence band edges, the position of the Fermi level at the semiconductor surface, the presence of the surface and bulk states, the potential drop in the space charge layer, and the semiconductor conductivity characteristics.

5. Conclusions

The product of the initial stage of the Mn(II) oxygenation catalyzed by hematite and FH NPs is dominated by Mn(II)CO_3-like species, which are attached to the catalysts surface as inner-sphere complexes. Within 3–5 h, these species partially transform into manganite (γ-MnOOH).

Smaller hematite NPs are surprisingly less effective (per unit surface area) catalysts of the Mn(II) oxygenation. The slowing down of the redox reaction causes reduction of hematite NPs. At the same time, FH NPs are not reduced. The effect is explained by the absence of kinetic obstacles for the Fe(II) ions produced by reactions (4) to be reoxidized by dissolved oxygen, which causes phase transformation of FH. These findings are attributed to the electrochemical mechanism of the redox activity of ferric (hydr)oxides given the nanosize-driven changes in both their electronic properties and the thermodynamic properties of the system.

Acknowledgments

Support of NSF under Grants # UCSB KK9157 and #0 749461 as well as of the Tata Research Development and Design Center, Pune, India is acknowledged. This work has used the shared experimental facilities that are supported primarily by the MRSEC program of NSF # DMR 0213574 and by the New York State Office of Science Technology and Academic Research (NYSTAR). IC thanks Prof. M.F. Hochella, Jr. for providing an opportunity to start this research.

Appendix A. Supplementary material

Supplementary data associated with this article can be found, in the online version, at doi:10.1016/j.jcat.2011.05.021.

References

[1] R.M. Cornell, U. Schwertmann, The Iron Oxide: Structure, Properties, Reactions and Uses, VCH, Weinheim, 1996.
[2] G.A. Waychunas, C.S. Kim, J.F. Banfield, Nanoparticulate iron oxide minerals in soils and sediments: unique properties and contaminant scavenging mechanisms, J. Nanopart. Res. 7 (2005) 409–433.
[3] V.H. Grassian, When size really matters: size-dependent properties and surface chemistry of metal and metal oxide nanoparticles in gas and liquid phase environments, J. Phys. Chem. C 112 (2008) 18303–18313.
[4] G. Rubasinghege, R.W. Lentz, M.M. Scherer, V.H. Grassian, Simulated atmospheric processing of iron oxyhydroxide minerals at low pH: roles of particle size and acid anion in iron dissolution, Proceedings of the National Academy of Sciences of the United States of America 107 (2010) 6628–6633.
[5] W. Zhang, M. Kalive, D.G. Capco, Y.S. Chen, Adsorption of hematite nanoparticles onto Caco-2 cells and the cellular impairments: effect of particle size, Nanotechnology 21 (2010) 355103.
[6] A. Navrotsky, Energetics of oxide nanoparticles, Int. J. Quant. Chem. 109 (2009) 2647–2657.
[7] I.V. Chernyshova, S. Ponnurangam, P. Somasundaran, On the origin of an unusual dependence of (bio)chemical reactivity of ferric hydroxides on nanoparticle size, Phys. Chem. Chem. Phys. 12 (2010) 14045–14056.
[8] D.M. Cwiertny, R.M. Handler, M.V. Schaefer, V.H. Grassian, M.M. Scherer, Interpreting nanoscale size-effects in aggregated Fe-oxide suspensions: reaction of Fe(II) with goethite, Geochim. Cosmochim Acta 72 (2008) 1365–1380.
[9] S. Bose, M.F. Hochella, Y.A. Gorby, D.W. Kennedy, D.E. McCready, A.S. Madden, B.H. Lower, Bioreduction of hematite nanoparticles by the dissimilatory iron reducing bacterium Shewanella oneidensis MR-1, Geochim. Cosmochim. Acta 73 (2009) 962–976.
[10] A.S. Madden, M.F. Hochella, A test of geochemical reactivity as a function of mineral size: manganese oxidation promoted by hematite nanoparticles, Geochim. Cosmochim. Acta 69 (2005) 389–398.
[11] J.Y. Ha, T.P. Trainor, F. Farges, G.E. Brown, Interaction of aqueous Zn(II) with hematite nanoparticles and microparticles. Part 1. EXAFS study of Zn(II) adsorption and precipitation, Langmuir 25 (2009) 5574–5585.
[12] D.M. Cwiertny, G.J. Hunter, J.M. Pettibone, M.M. Scherer, V.H. Grassian, Surface chemistry and dissolution of alpha-FeOOH nanorods and microrods: environmental implications of size-dependent interactions with oxalate, J. Phys. Chem. C 113 (2009) 2175–2186.
[13] I.V. Chernyshova, M.F. Hochella, A.S. Madden, Size-dependent structural transformations of hematite nanoparticles. 1. Phase transition, Phys. Chem. Chem. Phys. 9 (2007) 1736–1750.
[14] F.M. Michel, V. Barron, J. Torrent, M.P. Morales, C.J. Serna, J.F. Boily, Q.S. Liu, A. Ambrosini, A.C. Cismasu, G.E. Brown, Ordered ferrimagnetic form of ferrihydrite reveals links among structure, composition, and magnetism, Proceedings of the National Academy of Sciences of the United States of America 107 (2010) 2787–2792.
[15] F.M. Michel, L. Ehm, S.M. Antao, P.L. Lee, P.J. Chupas, G. Liu, D.R. Strongin, M.A.A. Schoonen, B.L. Phillips, J.B. Parise, The structure of ferrihydrite a nanocrystalline material, Science 316 (2007) 1726–1729.
[16] A. Manceau, Evaluation of the structural model for ferrihydrite derived from real-space modelling of high-energy X-ray diffraction data, Clay Minerals 44 (2009) 19–34.
[17] D.G. Rancourt, J.F. Meunier, Constraints on structural models of ferrihydrite as a nanocrystalline material, Am. Mineral. 93 (2008) 1412–1417.
[18] I.V. Chernyshova, An in situ FTIR study of galena and pyrite oxidation in aqueous solution, J. Electroanal. Chem. 558 (2003) 83–98.
[19] I.V. Chernyshova, S. Ponnurangam, P. Somasundaran, Tailoring (bio)chemical activity of semiconducting nanoparticles: critical role of deposition and aggregation, J. Am. Chem. Soc. 133 (2011) 9536–9544, doi:10.1021/ja202266g (2011).
[20] M. Kosmulski, The pH-dependent surface charging and the points of zero charge, J. Colloid Interface Sci. 253 (2002) 77–87.
[21] M. Kosmulski, pH-dependent surface charging and points of zero charge III. Update, J. Colloid Interface Sci. 298 (2006) 730–741.
[22] G.A. Parks, Isoelectric points of solid oxides solid hydroxides and aqueous hydroxo complex systems, Chem. Rev. 65 (1965) 177–198.
[23] D.S. Smith, F.G. Ferris, Specific surface chemical interactions between hydrous ferric oxide and iron-reducing bacteria determined using pK(a) spectra, J. Colloid Interface Sci. 266 (2003) 60–67.
[24] C.M. Su, D.L. Suarez, In situ infrared speciation of absorbed carbonate on aluminum and iron oxide, Clays Clay Miner. 45 (1997) 814–825.
[25] Y. Arai, D.L. Sparks, J.A. Davis, Effects of dissolved carbonate on arsenate adsorption and surface speciation at the hematite–water interface, Environ. Sci. Technol. 38 (2004) 817–824.
[26] S. Goldberg, C.T. Johnston, Mechanisms of arsenic adsorption on amorphous oxides evaluated using macroscopic measurements, vibrational spectroscopy, and surface complexation modeling, J. Colloid Interface Sci. 234 (2001) 204–216.
[27] T. Fujii, F.M.F. de Groot, G.A. Sawatzky, F.C. Voogt, T. Hibma, K. Okada, In situ XPS analysis of various iron oxide films grown by NO_2-assisted molecular-beam epitaxy, Phys. Rev. B 59 (1999) 3195–3202.
[28] T. SchedelNiedrig, W. Weiss, R. Schlogl, Electronic structure of ultrathin ordered iron oxide films grown onto Pt(111), Phys. Rev. B 52 (1995) 17449–17460.
[29] J. Junta, M.F. Hochella, Manganese(II) oxidation at mineral surfaces – a microscopic and spectroscopic study, Geochim. Cosmochim. Acta 58 (1994) 4985–4999.
[30] T. Yamashita, P. Hayes, Reply to Paparazzo, J. Electron Spectrosc. Related Phenomena 154 (2006) 41–42.
[31] S.H.R. Davies, J.J. Morgan, Manganese(II) oxidation-kinetics on metal-oxide surfaces, J. Colloid Interface Sci. 129 (1989) 63–77.
[32] J. Liu, D.M. Aruguete, M. Murayama, M.F. Hochella, Influence of size and aggregation on the reactivity of an environmentally and industrially relevant manomaterial (PbS), Environ. Sci. Technol. 43 (2009) 8178–8183.
[33] V.R. Galakhov, M. Demeter, S. Bartkowski, M. Neumann, N.A. Ovechkina, E.Z. Kurmaev, N.I. Logachevskaya, Y.M. Mukovskii, J. Mitchell, D.L. Ederer, Mn 3s exchange splitting in mixed-valence manganites, Phys. Rev. B 65 (2002) 113102.
[34] G.C. Allen, S.J. Harris, J.A. Jutson, J.M. Dyke, A study of a number of mixed transition-metal oxide spinels using X-ray photoelectron-spectroscopy, Appl. Surf. Sci. 37 (1989) 111–134.
[35] A.J. Nelson, J.G. Reynolds, G. Christou, Spin-state effects on the outer core-level multiplet structures for high-spin Mn molecular clusters, J. Appl. Phys. 93 (2003) 2536–2539.
[36] M. Oku, K. Hirokawa, S. Ikeda, X-ray photoelectron-spectroscopy of manganese-oxygen systems, J. Electron Spectrosc. Related Phenomena 7 (1975) 465–473.
[37] T. Uozumi, K. Okada, A. Kotani, R. Zimmermann, P. Steiner, S. Hufner, Y. Tezuka, S. Shin, Theoretical and experimental studies on the electronic structure of M(2)O(3) (M=Ti, V, Cr, Mn, Fe) compounds by systematic analysis of high-energy spectroscopy, J. Electron Spectrosc. Related Phenomena 83 (1997) 9–20.
[38] V. Dicastro, G. Polzonetti, XPS study of MnO oxidation, J. Electron Spectrosc. Related Phenomena 48 (1989) 117–123.
[39] A.J. Nelson, J.G. Reynolds, J.W. Roos, Core-level satellites and outer core-level multiplet splitting in Mn model compounds, J. Vacuum. Sci. Technol. A 18 (2000) 1072–1076.
[40] J. Vanelp, R.H. Potze, H. Eskes, R. Berger, G.A. Parks, Isoelectric points of solid oxides solid hydroxides and aqueous hydroxo complex systems, Chem. Rev. 65 (1965) 177–198.
[41] N.S. McIntyre, D.G. Zetaruk, X-ray photoelectron spectroscopic studies of iron-oxides, Anal. Chem. 49 (1977) 1521–1529.
[42] A.P. Grosvenor, B.A. Kobe, M.C. Biesinger, N.S. McIntyre, Investigation of multiplet splitting of Fe 2p XPS spectra and bonding in iron compounds, Surf. Interface Anal. 36 (2004) 1564–1574.

[43] S. Poulin, R. Franca, L. Moreau-Belanger, E. Sacher, Confirmation of X-ray photoelectron spectroscopy peak attributions of nanoparticulate iron oxides, using symmetric peak component line shapes, J. Phys. Chem. C 114 (2010) 10711–10718.

[44] T. Droubay, S.A. Chambers, Surface-sensitive Fe 2p photoemission spectra for alpha-Fe_2O_3(0001): the influence of symmetry and crystal-field strength, Phys. Rev. B 64 (2001) 205414.

[45] F. Labat, I. Ciofini, C. Adamo, Modeling ZnO phases using a periodic approach: from bulk to surface and beyond, J. Chem. Phys. 131 (2009) 044708.

[46] W. Stumm, J.J. Morgan, Aquatic Chemistry, third ed., Wiley, New York, 1996.

[47] W. Stumm, The inner-sphere surface complex – a key to understanding surface reactivity, in: C.P. Huang, C.R. Omelia, J.J. Morgan (Eds.), Aquatic Chemistry – Interfacial and Interspecies Processes, Amer. Chemical Soc., Washington, 1995, pp. 1–32.

[48] J. Lützenkirchen (Ed.), Surface Complexation Modeling, in: Interface Science and Technology, Elsevier, Amsterdam, 2006, p. 652.

[49] M.A. Schoonen, D.R. Strongin, Catalysis of electron transfer reactions at mineral surfaces, in: V.H. Grassian (Ed.), Environmental Catalysis, Taylor&Fransis Group, Boca Raton, FL, 2005, pp. 37–60.

[50] W. Stumm, Catalysis of redox processes by hydrous oxide surfaces, Croat. Chem. Acta 70 (1997) 71–93.

[51] B. Wehrli, B. Sulzberger, W. Stumm, Redox processes catalyzed by hydrous oxide surfaces, Chem. Geol. 78 (1989) 167–179.

[52] J. Klausen, S.P. Trober, S.B. Haderlein, R.P. Schwarzenbach, Reduction of substituted nitrobenzenes by Fe(II) in aqueous mineral suspensions, Environ. Sci. Technol. 29 (1995) 2396–2404.

[53] S. Ponnurangam, I.V. Chernyshova, P. Somasundaran, Effect of co-adsorption of electrolyte ions on the stability of inner-sphere complexes, J. Phys. Chem. C 114 (2010) 16517–16524.

[54] J.A. Davis, J.O. Leckie, Effect of adsorbed complexing ligands on trace-metal uptake by hydrous oxides, Environ. Sci. Technol. 12 (1978) 1309–1315.

[55] B.M. Reddy, Redox properties of metal oxides, in: J.L.G. Fierro (Ed.), Metal Oxides: Chemistry and Applications, CRC Group Taylor and Francis Group, LLC, Boca Raton, FL, 2006, pp. 215–246.

[56] W.J. Royea, A.M. Fajardo, N.S. Lewis, Fermi golden rule approach to evaluating outer-sphere electron-transfer rate constants at semiconductor/liquid interfaces (vol 101, pg 11152, 1997), J. Phys. Chem. B 102 (1998) 3653.

[57] R. Woods, in: J.O. Bockris, B.E. Conway, R.E. White (Eds.), Modern Aspects of Electrochemistry, Plenum Press, New York, 1996, pp. 401–453.

[58] I.V. Chernyshova, Anodic processes on a galena (PbS) electrode in the presence of n-butyl xanthate studied FTIR-spectroelectrochemically, J. Phys. Chem. B 105 (2001) 8185–8191.

[59] I.V. Chernyshova, Anodic oxidation of galena (PbS) studied FTIR-spectroelectrochemically, J. Phys. Chem. B 105 (2001) 8178–8184.

[60] D.D.H. Bhushan, N. Zope, Matthew Neurock, Robert J. Davis, Reactivity of the gold/water interface during selective oxidation catalysis, Science 330 (2010) 74–78.

[61] T. Lindgren, L. Vayssieres, H. Wang, S.-E. Lindquist, Photo-oxidation of water at hematite electrodes, in: A.I. Kokorin, D.W. Bahnemann (Eds.), Chemical Physics of Nanostructured Semiconductors, VSP-International Science Publishers, 2003, pp. 83–110.

[62] C. Noguera, A. Pojani, P. Casek, F. Finocchi, Electron redistribution in low-dimensional oxide structures, Surface Sci. 507 (2002) 245–255.

[63] R. Morrison, Electrochemistry at Semiconductor and Oxidized Metal Electrodes, Plenum Press, New York, 1980.

[64] A. Duret, M. Gratzel, Visible light-induced water oxidation on mesoscopic alpha-Fe_2O_3 films made by ultrasonic spray pyrolysis, J. Phys. Chem. B 109 (2005) 17184–17191.

[65] R.R. Rangaraju, A. Panday, K.S. Raja, M. Misra, Nanostructured anodic iron oxide film as photoanode for water oxidation, J. Phys. D – Appl. Phys. 42 (2009) 135303.

[66] L. Xiong, H.W. Jiang, D.Z. Wang, Preparation and characterization of polyacrylamide-modified Fe_3O_4 magnetic nanoparticles, Acta Polym. Sinica (2008) 259–265.

[67] D.D. Boland, R.N. Collins, T.E. Payne, T.D. Waite, Effect of amorphous Fe(III) oxide transformation on the Fe(II)-mediated reduction of U(VI), Environ. Sci. Technol. 45 (2011) 1327–1333.

[68] S.V. Yanina, K.M. Rosso, Linked reactivity at mineral-water interfaces through bulk crystal conduction, Science 320 (2008) 218–222.

[69] Y.S. Hwang, J.J. Lenhart, Adsorption of C4-dicarboxylic acids at the hematite/water interface, Langmuir 24 (2008) 13934–13943.

[70] S.-Y. Shih-Yun Chen, A. Gloter, A. Zobelli, L. Wang, C.-H. Chen, C. Collie, Electron energy loss spectroscopy and ab initio investigation of iron oxide nanomaterials grown by a hydrothermal process, Phys. Rev. B 79 (2009) 104103.

[71] K.M. Rosso, S.V. Yanina, C.A. Gorski, P. Larese-Casanova, M.M. Scherer, Connecting observations of hematite (alpha-Fe_2O_3) growth catalyzed by Fe(II), Environ. Sci. Technol. 44 (2010) 61–67.

[72] A.G.B. Williams, M.M. Scherer, Spectroscopic evidence for Fe(II)–Fe(III) electron transfer at the iron oxide–water interface, Environ. Sci. Technol. 38 (2004) 4782–4790.

[73] A.J. Anschutz, R.L. Penn, Reduction of crystalline iron(III) oxyhydroxides using hydroquinone: influence of phase and particle size, Geochem. Trans. 6 (2005) 60–66.

[74] D. Nykypanchuk, M.M. Maye, D. van der Lelie, O. Gang, DNA-guided crystallization of colloidal nanoparticles, Nature 451 (2008) 549–552.

[75] F. Gaboriaud, J. Ehrhardt, Effects of different crystal faces on the surface charge of colloidal goethite (alpha-FeOOH) particles: an experimental and modeling study, Geochim. Cosmochim. Acta 67 (2003) 967–983.

[76] S.E. Mason, C.R. Iceman, K.S. Tanwar, T.P. Trainor, A.M. Chaka, Pb(II) adsorption on isostructural hydrated alumina and hematite (0001) surfaces: a DFT study, J. Phys. Chem. C 113 (2009) 2159–2170.

[77] S.E. Mason, T.P. Trainor, A.M. Chaka, Hybridization-reactivity relationship in Pb(II) adsorption on alpha-Al_2O_3–water interfaces: a DFT Study, J. Phys. Chem. C 115 (2011) 4008–4021.

[78] J.D. Hem, Redox processes at surfaces of manganese oxide and their effects on aqueous metal ions, Chem. Geol. 21 (1978) 199–218.

[79] H.O. Finklea, Electron transfer, in: A.J. Bard, M. Stratmann (Eds.), Encyclopedia of Electrochemistry, Wiley-VCH, Weinheim, 2007, pp. 623–650.